# 2.6 OBSERVATION SENSITIVITY AND THE MIX OF OBSERVING SYSTEMS

Nancy L. Baker and Rolf H. Langland*
Naval Research Laboratory, Monterey, California

## 1. INTRODUCTION

The adjoint of the NRL Atmospheric Variational Data Assimilation System (NAVDAS) is used to compute the sensitivity of a scalar cost function $J$ to the observations available in an analysis valid at 00 UTC 7 February 1999. This case corresponds to the largest 72-h Navy Operational Global Analysis and Forecast System (NOGAPS) forecast error verifying over the western United States and Canada during a three-year period from 1997 – 1999. Synoptically, the case involves the failure to forecast a strong trough along the U.S. West Coast, with a blocking ridge upstream in the north Pacific.

The analysis sensitivity gradients are computed using an energy-weighted forecast error cost function $J$ for the NOGAPS forecast starting from the initial time of 00 UTC 7 February 1999 and verifying 72 h later at 00 UTC 10 February 1999.

The observation and background adjoint sensitivity theory, along with several simple examples to illustrate and explain the observation and background sensitivity, is presented in Baker and Daley (1999), and is explored in detail in Baker (2000). For completeness, the definition for the observation adjoint sensitivity is included here; *viz.,*

$$\partial J/\partial \mathbf{y} = (\mathbf{H}\mathbf{P}_b\mathbf{H}^T + \mathbf{R})^{-1}\mathbf{H}\mathbf{P}_b\,\partial J/\partial \mathbf{x}_a \qquad \textbf{(1)}$$

where $\mathbf{y}$ is the vector of observations, and $\mathbf{x_a}$ and $\mathbf{x_b}$ are the analysis and background vectors, respectively. The matrix $\mathbf{H}$ is the Jacobian matrix corresponding to the forward operator $H\{x_b\}$ linearized about the background state vector. The background error covariance is given by $\mathbf{P}_b$, while the observation error covariance is denoted by $\mathbf{R}$. This procedure is similar to that described by Dornbecher et al. (2000).

* Corresponding author address: Dr. Rolf Langland, Naval Research Laboratory, Global Modeling Section, 7 Grace Hopper Ave., Monterey, California 93943-5502

## 2. MEASURES OF POTENTIAL OBSERVATION FORECAST IMPACT

The change in the forecast aspect $J$ is defined as the projection of the analysis error ($\varepsilon_a$) onto the analysis sensitivity gradient, or

$$\delta J = \varepsilon_a^T \frac{\partial J}{\partial \mathbf{x}_a}. \qquad \textbf{(2)}$$

After considerable manipulation (see Baker (2000) for details), the expected variance of the change in the forecast aspect due to the background and the observations may be written

$$\left\langle (\delta J)^2 \right\rangle = \left(\frac{\partial J}{\partial \mathbf{x_a}}\right)^T \mathbf{P}_b \frac{\partial J}{\partial \mathbf{x_a}} - \left(\frac{\partial J}{\partial \mathbf{y}}\right)^T (\mathbf{H}\mathbf{P}_b\mathbf{H}^T + \mathbf{R})\frac{\partial J}{\partial \mathbf{y}}$$
$$= \left\langle (\delta J)^2 \right\rangle_b - \left\langle (\delta J)^2 \right\rangle_o . \qquad \textbf{(3)}$$

The second term on the right-hand side of (3) may be interpreted as the reduction in the expected variance of the change in $J$ due to the observations.

The reduction of the expected variance of $\delta J$ computed from (3) is a scalar number, which may be computed for specified subsets of observations, such as radiosondes, cloud-drift winds, or different adaptive observation configurations, so that their relative contributions can be assessed. For targeting applications, $\left\langle (\delta J)^2 \right\rangle_o$ can be used to rank different adaptive observation configurations according to their potential impact on $J$. It is important to note that the actual impact (i.e., sign of $\delta J$) cannot be determined except by assimilating the observations and computing the forecast. It is also important to realize that the term $(\mathbf{H}\mathbf{P}_b\mathbf{H}^T + \mathbf{R})$ in (3) always involves the entire set of observations, so that changing the properties (location or assumed error variance) of even one observation will change the scalar measure for all other observations.

## 3. TARGETING STRATEGIES WITH THE NAVDAS ADJOINT

The observations are derived from the global meteorological reports available operationally at Fleet Numerical Meteorology and Oceanography Center (FNMOC) and are valid for a six-hour window centered on the target time. For this particular case, the set of observations also include 11 dropsondes deployed by the NOAA G-IV aircraft as part of the Winter Storm Reconnaissance (WSR) Program. While the actual observed values and background fields are not required to compute the observation and background sensitivities, the observed values and background fields are required for the NAVDAS analysis pre-processing and observation quality control algorithms. In this way, the NAVDAS adjoint computes the sensitivities to the actual observations used by the NAVDAS assimilation cycle.

The analysis sensitivities $\partial J/\partial \mathbf{x}_a$ for the 850- and 500-hPa levels are shown in Figs. 1 and 2, respectively. The high amplitude, small-scale temperature analysis sensitivity gradient sub-structure centered at about 43°N and 155°W in Fig. 1c has maximum amplitude near 850 hPa and weakens as it tilts westward with increasing height (e.g., Fig. 2c). In contrast, the moderate amplitude, large-scale temperature analysis sensitivity gradient sub-structure centered at about 40°N and 175°W in Fig. 2c has maximum amplitude near 500 hPa and strong westward (baroclinic) vertical tilt. The v-wind analysis sensitivity gradient extrema have similar amplitude for the two pressure levels and also tend to tilt westward with increasing height. The largest amplitudes of the 850 hPa u-wind analysis sensitivity gradient are associated with the temperature and v-wind analysis sensitivity gradient extrema, while the largest amplitudes at 500 hPa are associated with the northern branch of the subtropical jet south of 40°N.

Here, three hypothetical targeted observing strategies using dropsondes, and the actual WSR G-IV flight are examined. The first hypothetical deployment is for an aircraft departing from Shemya Island (52.72°N, 174.10°W), and allows for sampling of the mid-Pacific Ocean. Each of the 20 dropsondes is assumed to measure temperature, wind speed and direction at 50 hPa increments from 200 and 1000 hPa with an accuracy equivalent to a conventional radiosonde in NAVDAS. The second hypothetical flight track (also with 20 dropsondes in a backwards "N" pattern) is designed to sample the extrema and gradients of the high-amplitude, small-scale temperature analysis sensitivity pattern at 850 hPa (see Fig. 1).

The third hypothetical targeting strategy utilizes the new driftsonde observing system that is being developed by NCAR as a candidate observing system for the proposed THORPEX experiment. The driftsonde carrier balloon ascends to between 50 and 100 hPa and drifts with the prevailing stratospheric winds for up to five days. Dropsondes may be released at specified intervals. The dropsonde observations are collected and sent via satellite to ground processing stations for real-time dissemination on the Global Telecommunication System.

The hypothetical driftsonde locations valid for 00 UTC 7 February 1999 were computed by assuming that the driftsonde carrier balloons were launched at 12-h intervals beginning with 00 UTC 2 February 1999 from 13 launch sites along the east coast of Asia. The 50-hPa FNMOC operational wind analyses were used to advect the carrier balloons. The driftsonde locations over the oceans are assumed to correspond to dropsonde releases. Each dropsonde is assumed to measure temperature, wind speed and direction at 50 hPa increments from 100 and 1000 hPa with an accuracy equivalent to a conventional radiosonde in NAVDAS. This hypothetical driftsonde network provides 45 dropsonde profiles, or more than twice as many adaptive observations as those from the G-IV flight centered on 00 UTC 7 February 1999.

## 4. RESULTS

The reduction in the expected variance of the change in the forecast aspect, or $\left\langle (\delta J)^2 \right\rangle_o$ is computed from (3) using all observations from the regular and targeted components of the global observing network. Results for radiosondes and dropsondes in the G-IV deployment case are shown in Fig. 3. The reduction in $\left\langle (\delta J)^2 \right\rangle_o$ is largest for the three Alaskan radiosonde stations of Shemya Island, St. Paul Island (57.15°N, 170.22°W), and Sand Point (55.20°N, 167.72°W), and occur because these radiosonde stations are relatively isolated and are in regions where the analysis sensitivity gradients are strong (see Baker (2000)). In contrast, the reduction in $\left\langle (\delta J)^2 \right\rangle_o$ from the G-IV dropsondes is modest, with the largest contribution from the more isolated dropsonde at the apex of the inverted "V" where the temperature and wind analysis sensitivity gradients are relatively large in amplitude and scale. In general, the dropsondes along the western flight leg coincide with stronger temperature and wind analysis sensitivity gradients than the dropsondes along the eastern flight leg and make correspondingly larger reductions in $\left\langle (\delta J)^2 \right\rangle_o$.

The reductions in $\left\langle (\delta J)^2 \right\rangle_o$ for the hypothetical Shemya-based targeting flight, the

backwards "N" deployment, and the driftsonde network are shown in Figs. 4 to 6, respectively. The radiosondes from Shemya, St. Paul Island, and Sand Point again dominate the change in $\left\langle (\delta J)^2 \right\rangle_o$, although the contribution of these radiosondes is lessened when adaptive dropsondes are nearby (e.g., Figs. 4 and 6). Overall, the largest reductions in $\left\langle (\delta J)^2 \right\rangle_o$ occur for the hypothetical Shemya flight path dropsondes (Fig. 4) and for the driftsonde-deployed dropsonde network (Fig. 6). For the driftsonde-deployed dropsonde network (Fig. 6), the strongest reductions in $\left\langle (\delta J)^2 \right\rangle_o$ occur from the dropsondes in the mid-Pacific Ocean near large horizontal scale and amplitude analysis sensitivity gradients. Both of these dropsonde networks sample the large amplitude, large-scale analysis temperature and wind sensitivity gradients in the mid-Pacific Ocean in Figs. 1-2.

It is worth noting the results for the backwards "N" deployment (Fig. 5). Since features similar to the high-amplitude, small-scale temperature analysis sensitivity gradient sub-structures (Fig. 1c) were often selected as targets during FASTEX and NORPEX, the flight path in Fig. 5 was designed to sample both the extrema and the gradients, with the *a priori* expectation that such a deployment would maximize the observation sensitivity. However, the reductions in $\left\langle (\delta J)^2 \right\rangle_o$ from this dropsonde configuration are quite small, which indicates that the sensitivity to these observations is also small. These results support the conclusions from Baker and Daley (2000) that the data assimilation system is comparatively insensitive to the observations when the length scale of the analysis sensitivity sub-structures is smaller than the background error correlation length scale. While it is tempting to speculate that the majority of the observations in this deployment are unnecessary and may be eliminated, the results from Baker (2000) suggest that, for small-scale analysis sensitivity gradients, the observation sensitivity increases as the observation density increases. Consequently, more observations may be required to sample this small-scale analysis sensitivity gradient.

## 5. SUMMARY AND DISCUSSION

Baker and Daley (1999) and Baker (2000) demonstrated that the observation sensitivity is largest when the analysis sensitivity gradients and the background error correlations have similar length scales. Observation sensitivity is also maximized when the observation is assumed to be accurate relative to the background, and the observation is relatively isolated or an abrupt discontinuity in the observation density coincides with moderate to large amplitude analysis sensitivity gradients.

For the examples presented in this paper, the adjoint of the NAVDAS data assimilation system is used to compute the sensitivity of $J$ to the observations available for an analysis valid at 00 UTC 7 February 1999. A scalar measure of the reduction in the expected variance in the change of the forecast aspect $J$, which uses the observation sensitivities computed for the entire global set of observations, was introduced. This measure, $\left\langle (\delta J)^2 \right\rangle_o$ was used to evaluate the implied reductions in forecast error for different hypothetical adaptive observation-targeting strategies. Overall, the largest reductions in $\left\langle (\delta J)^2 \right\rangle_o$ are produced by observations that are relatively isolated and located near high-amplitude, large-scale analysis sensitivity gradients. The two hypothetical targeting deployments with the largest implied forecast error reductions are the Shemya-based targeting flight and the driftsonde-deployed dropsonde network that sample the large-amplitude, large-scale analysis temperature and wind sensitivity gradients in the mid-Pacific Ocean. Large implied reductions in errors in this case also occur for several of the Alaskan radiosonde reports.

These results suggest that targeting decisions based solely on the analysis sensitivity gradients or associated singular vectors may be substantially different from targeting decisions that also consider the adjoint of the data assimilation system.

## 6. REFERENCES


Baker, N.L., and R. Daley, 2000: Observation and background adjoint sensitivity in the adaptive observation-targeting problem. *Q.J.R. Meteorol. Soc*., **126**, 1431-1454.

Baker, N.L., 2000: Observation adjoint sensitivity and the adaptive observation-targeting problem. Ph.D. Dissertation. Naval Postgraduate School, Monterey, CA, 267 pp.

Dornbecher, A., T. Bergot, and F. Bouttier, 2000: Sensitivity to observations and targeted observations. *4th Symposium on Integrated Observing Systems*. 9-14 January 2000, Long Beach, CA., 200-203.

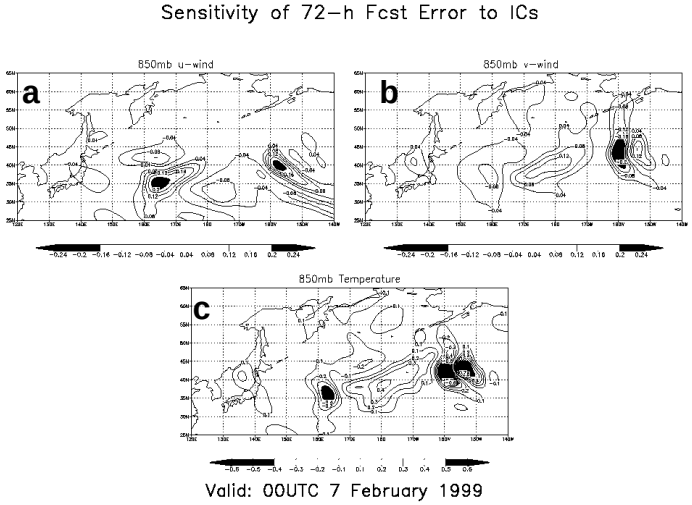


Figure 1. Sensitivity of the 72-h NOGAPS energy-weighted forecast error with respect to the 850-hPa initial (a) u-wind component, (b) v-wind component, and (c) temperature fields valid at the targeted observing time of 00 UTC 7 February 1999. The forecast verification area (not shown) is centered over the western United States and Canada (30 $^{o}$N – 60$^{o}$N and 150$^{o}$W – 100$^{o}$W). Units of sensitivity are J kg$^{-1}$ m$^{-1}$ s (a,b), and J kg$^{-1}$ deg$^{-1}$ (c).

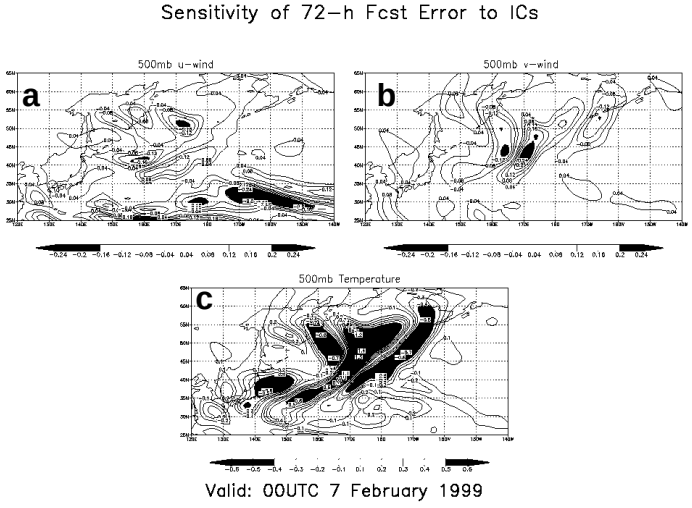


Figure 2. As in Fig. 1, except for the sensitivity of the 72-h NOGAPS energy-weighted forecast error with respect to the 500-hPa initial (a) u-wind component, (b) v-wind component, and (c) temperature fields valid at the targeted observing time of 00 UTC 7 February 1999. Units of sensitivity are J kg$^{-1}$ m$^{-1}$ s (a,b), and J kg$^{-1}$ deg$^{-1}$ (c).

*Reduction in expected variance due to G-IV dropsondes: 40,010 (J kg$^{-1}$)$^2$*

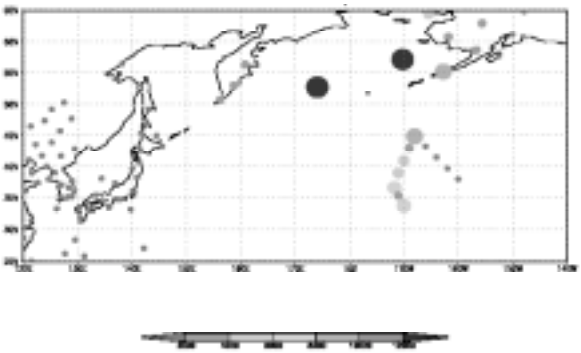

Figure 3. The reduction in the expected variance of the change in the 72-h forecast error $\left\langle (\delta J)^2 \right\rangle_o$ computed for all observations for the **control plus G-IV targeting (CTL+GIV) case**, and plotted for the radiosonde and dropsonde observations. The circle size is proportional to $\left\langle (\delta J)^2 \right\rangle_o$, units are (J kg$^{-1}$)$^2$.

*Reduction in expected variance due to "backwards N" dropsonde pattern: 11,231 (J kg$^{-1}$)$^2$*

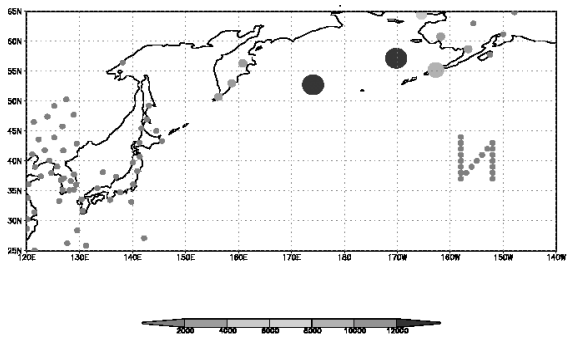

Figure 5. As in Fig. 3, except for the reduction in the expected variance of the change in the 72-h forecast error $\left\langle (\delta J)^2 \right\rangle_o$ computed for all observations for the **control plus the "backwards N" (CTL+c4) case**, and plotted for the radiosonde and dropsonde observations.

*Reduction in expected variance due to G-IV "Shemya deployment": 90,916 (J kg$^{-1}$)$^2$*

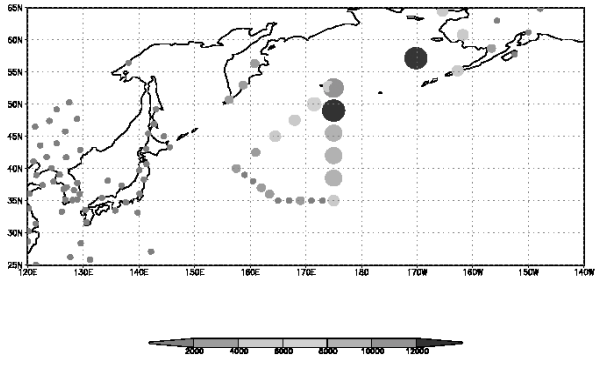

Figure 4. As in Fig. 3, except for the reduction in the expected variance of the change in the 72-h forecast error $\left\langle (\delta J)^2 \right\rangle_o$ computed for all observations for the **control plus hypothetical targeting deployment from Shemya (CTL+s1) case**, and plotted for the radiosonde and dropsonde observations.

*Reduction in expected variance due to hypothetical driftsonde network: 129,539 (J kg$^{-1}$)$^2$*

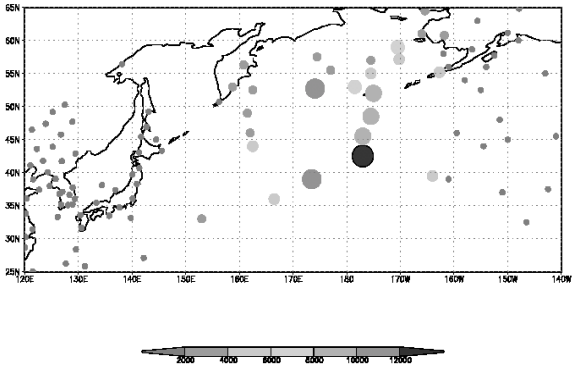

Figure 6. As in Fig. 3, except for the reduction in the expected variance of the change in the 72-h forecast error $\left\langle (\delta J)^2 \right\rangle_o$ computed for all observations for the **control plus hypothetical driftsonde-deployed dropsondes (CTL+d1) case**, and plotted for the radiosonde and driftsonde-deployed dropsonde observations.